Mechanism and Machine Theory 167 (2022) 104568

Contents lists available at ScienceDirect

Mechanism and Machine Theory

journal homepage: www.elsevier.com/locate/mechmt

Research paper

intraOcular RoBotic Interventional System (iORBIS): Mechanical design for distally-actuated instrument insertion and automatic tool change☆

Cheng-Wei Chen *, Hsing-Chi Chen, Hung-Yu Yang, Xiang-Yan Zeng, Xian-Hao Wu, Po-Chih Chen

Electrical Engineering, National Taiwan University, No. 1, Sec. 4, Roosevelt Rd., Taipei, 10617, Taiwan

ARTICLE INFO

Keywords:
Surgical robot
Remote center-of-motion
Assembly error estimation
Automatic instrument changer

ABSTRACT

Parallelogram-based remote center-of-motion (RCM) mechanisms have been intensively deployed in intraocular surgical robots. However, the actuation of instrument linear movement in conventional parallelogram-based RCM mechanisms is mostly done by a linear actuator installed near the end-effector. This design inevitably increases the volume and mass on the patient side of the robot. In this work, we present a novel parallelogram-based RCM mechanism that allows distally-actuated instrument insertion and retraction. Compared to the existing work, the proposed mechanism decouples the translational motion from other rotational degrees of freedom with a simple design. This feature may further enhance the safety of delicate procedures like sub-retinal injection. Based on the kinematic analysis, a method is developed for assembly error estimation and correction. Moreover, an automatic instrument changer is integrated with the robotic manipulator. Experiments are conducted on a prototypical system to validate the feasibility of the proposed design. The RCM precision is shown as better than 0.5 mm. The time required for switching surgical instruments is demonstrated as less than 10 s.

1. Introduction

With the benefits of a small incision and precise manipulation, robot-assisted microsurgery has been extensively investigated in recent years [1–3]. Particularly, advanced robotic systems have been developed, such as the steady-hand eye robot [4–6], MICRON [7,8], RAM!S [9–11], IRISS [12,13], and Preceyes surgical system [14,15], to assist intraocular microsurgery that requires the tool-tip positioning accuracy to be better than 10 μm [16]. In 2018, the first-in-human study of remotely operated retinal surgery was successfully performed using the Preceyes surgical system [15]. Besides, medical imaging modalities are integrated with the robotic manipulator for autonomous surgical navigation and guidance. For instance, guided by preoperative and intraoperative optical coherence tomography (OCT) images, the IRISS is capable of performing semi-automated lens removal from ex vivo pig eyes [17,18]. Despite the advances in applying robotic technologies to intraocular surgical procedures, developing a multifunctional robotic surgical system remains challenging because of the confined workspace.

During intraocular microsurgery, the incision port on the patient's eye imposes a kinematic constraint on the degrees of freedom (DoFs) of the surgical instrument. This requirement is usually fulfilled by mechanically constrained remote center-of-motion (RCM)

☆ This work was supported in part by the Ministry of Science and Technology in Taiwan (Young Scholar Fellowship MOST 108-2636-E-002-007 and 109-2636-E-002-032).

* Corresponding author.
E-mail address: cwchenee@ntu.edu.tw (C.-W. Chen).

https://doi.org/10.1016/j.mechmachtheory.2021.104568
Received 26 February 2021; Received in revised form 10 August 2021; Accepted 21 September 2021
Available online 8 October 2021

mechanisms [19–22]. Several RCM mechanisms featuring a compact and lightweight design have been proposed not only for eye surgery, but also for general minimal invasive surgery. For example, the lightweight endoscope robot (LER) [23] applies a spherical RCM mechanism to enable 3-DoF motions about the RCM. Similar to the LER, the spherical mechanisms are also applied to manipulate a surgical instrument [24,25]. On the other hand, the parallelogram-based RCM is more popular for robot-assisted intraocular surgery because it has a smaller footprint and provides a relatively large moving range over spherical RCM mechanisms [26]. However, in most existing intraocular surgical robots applying the parallelogram-based RCM [5,14], the insertion and retraction of the surgical instrument are directly driven by a linear actuator installed near the end-effector, resulting in increased volume, mass, inertia, and vibration. The bulky end-effector also hinders the integration with other critical subsystems such as a microscope and a tool changer.

To date, only a few parallelogram-based RCM mechanisms allow distal actuation of tool translation. Directly placing the insertion actuator distal to the parallelogram would invalid the mechanically constrained RCM. The conventional parallelogram-based RCM mechanism is revised, so that tool translation is actuated by folding additional parallelograms near the base [27,28]. Similar design concepts are also proposed in [29–32]. In these revised parallelogram-based RCM mechanisms, translational and rotational motions of the instrument are coupled. The insertion motion requires synchronous actuation of more than one motor. Although coupled kinematics are common in robotic systems, unnecessary risks are posed in some delicate surgical procedures like sub-retinal injection, where the injector is first oriented and then stably inserted at the target tissue [11]. The coupling error caused by kinematic inaccuracies and asynchronous motion control may induce undesired motions in multiple DoFs to damage the surrounding tissues during the needle insertion.

In recent studies, the coupled motions in the revised parallelogram-based RCM mechanisms are successfully decoupled [33,34]. However, additional parallelograms still exist in their results. Compared with the conventional parallelogram-based RCM mechanism, higher design complexity may cause manufacturing errors [35] and human errors in assembly operations [36]. Hence, it is desirable to simplify the mechanism design while keeping the distally-actuated tool translation and decoupled kinematics.

In this work, we develop a robotic surgical system — the intraOcular RoBotic Interventional System (iORBIS). A novel RCM mechanism is proposed such that the tool translation is directly driven by a linear ball screw actuator mounted near the base. A double-prismatic joint that constrains the excessive DoF is included to sustain the parallelogram-based RCM mechanism. Besides, the actuation of translational and rotational motions is decoupled. Thus, the kinematics and control of the robotic manipulator are identical to those with a conventional parallelogram-based RCM mechanism.

By leveraging the simplified design near the end-effector, the iORBIS is capable of automatic instrument changing. This function further enhances the time-efficiency of robot-assisted surgical tasks in where switching of surgical instruments is required. Automatic instrument changing is an important feature but rarely implemented in the existing robotic surgical systems. [37] reports that the ophthalmic instrument is changed, on average, every two minutes during a surgical task. Thus, it is essential to have the surgical robot quickly and precisely switch the surgical instrument. In most of the existing systems [9,38], customized instrument fixture design for manual instrument changing is typically applied. In the steady-hand eye robot [39], a variety of instruments is redesigned such that both axial fixation and rotation are achieved by a unified interface between the tool and the end-effector. [37] attaches adapters to the instruments to reduce the cost of redesigning the surgical instruments. The time required to switch an instrument manually is around 12 s.

To enable automatic instrument changing, the IRISS [13], the Vanderbilt system [40], and the design of Preceyes surgical system [41] allow the installation of multiple tools on the end-effector. However, these designs accompanied by a tool switching mechanism inevitably increase the complexity and volume of the manipulator. In fact, automatic tool changing is a mature technology in industrial applications [42,43]. This function has also been implemented in the existing robotic systems for general surgery [44]. However, due to the volume constraint in ophthalmic microsurgery, no automatic instrument changing system has been implemented on an intraocular surgical robot with a parallelogram-based RCM.

The main contributions of this work are threefold:

1. Proposing a novel RCM mechanism that directly actuates instrument insertion and retraction while avoiding the installation of a linear drive or cable-pulley scheme near the end-effector. The effect and treatment of assembly errors in the proposed RCM mechanism are also analyzed.
2. Designing an automatic instrument changer to enable quick and precise switching of commercially available instruments within 10 s.
3. Evaluating the feasibility and performance of the prototypical system. The RCM precision is shown as better than 0.5 mm.

The rest of this article is organized as follows: the proposed RCM mechanism and kinematic analysis are provided in Section 2; the mechanical designs for the robotic manipulator and automatic instrument changer are described in Section 3; Section 4 demonstrates the evaluation of the prototypical system; the concluding remarks are given in Section 5.

2. Proposed mechanism and kinematic analysis

In this section, a novel RCM mechanism with distally-actuated instrument translation is proposed. The kinematic model of the robotic manipulator is derived. The formulation, implication, and estimation of the assembly errors are then analyzed.

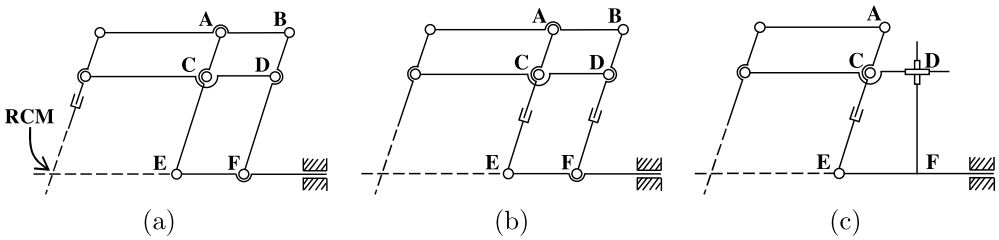

Fig. 1. Mechanism synthesis for the iORBIS robotic manipulator. (a) The conventional double-parallelogram RCM mechanism. (b) The linear actuator in subfigure (a) is moved to the segments CE and DF. (c) The proposed RCM mechanism, where the segment DF in subfigure (b) is fixed vertically and the rotary joint D is replaced with a double-prismatic joint.

2.1. Conceptual design

The mechanism synthesis of the robotic manipulator is illustrated in Fig. 1. Fig. 1(a) shows the conventional double-parallelogram RCM mechanism. Typically, the RCM is aligned with the incision port. Two rotational DoFs are actuated by attaching motors at the rotary joints near the base. A linear actuator is installed near the end-effector to actuate the tool insertion and retraction. In the conventional double-parallelogram RCM mechanism, all of the motion axes are decoupled. The tool-tip position is usually represented in the polar coordinate system, which directly maps the desired motion to the actuated DoFs.

The tool translation can be remotely actuated by installing two linear actuators at the segments CE and DF, respectively (Fig. 1(b)). However, this arrangement creates an excessive DoF if two linear actuators are not synchronous. It is very challenging to synchronize the motion of these two actuators even as both actuators are identical. Different inertia and payloads cause unbalanced motions and, thus, diminish the RCM precision.

The key of the double-parallelogram RCM mechanism is that the segments AB, CD, and EF must be parallel. The parallelogram constraint is satisfied in this work by adding a double-prismatic joint at joint D (Fig. 1(c)). The segment DF is vertically fixed on the baseline EF. In this mechanism, the segment CD is always parallel to EF, and, therefore, only a single linear actuator is required. The tool translation is directly driven by the linear actuator attached to CE. The actuation of the other two rotational motions is identical to that in the conventional double-parallelogram RCM mechanism. Thus, all of the motion axes are still decoupled in the proposed RCM mechanism.

The performance comparison between the proposed RCM mechanism and the conventional double-parallelogram RCM mechanism is made using a finite element simulation. The models of both RCM mechanisms are as illustrated in Fig. 2(a). In the simulation, force impulses are applied to the linear actuators, emulating the reaction forces caused by tool insertion accelerated from 0 to 100 mm/s within 0.01 s and deaccelerated at the same rate after 0.1 s. The maximal deformations of the mechanisms and the displacements of the tool-tips are shown in Figs. 2(a) and 2(b), respectively. The results indicate that the tool-tip displacement caused by tool acceleration is improved by 20 times using the proposed RCM mechanism. As will be shown in the next subsection, the kinematic model of the proposed RCM mechanism is identical to the conventional double-parallelogram RCM mechanism. Therefore, both RCM mechanisms own the same workspace and manipulability.

2.2. Kinematic model and assembly errors

The definition of the coordinate frames and kinematic parameters for the iORBIS robotic manipulator is illustrated in Fig. 3. The values of the kinematic parameters are listed in Table 1. The fixed reference frame (X_o, Y_o, Z_o) is located at the ideal RCM of the proposed mechanism. The frame (X_t, Y_t, Z_t) is located at the tool-tip.

Ideally, the tool-tip rotates about the X_o- and Y_o-axis as the rotary joint $\theta_1 \in \mathbb{R}$ and $\theta_2 \in \mathbb{R}$ revolves, respectively. When $\theta_1 = \theta_2 = 0$, the robot is at the initial position where Z_t is parallel to Z_o. The prismatic joint $d_3 \in \mathbb{R}$ determines the depth of insertion through the RCM. The rotary joint $\theta_4 \in \mathbb{R}$ indicates the rotational angle of the instrument about its centerline. By controlling these joints, the tool-tip is driven to the desired pose.

Due to the complexity of the parallelogram mechanism, assembly errors may appear and have significant effects on the RCM performance. Specifically, three critical errors are considered in this work, namely the angular misalignment error $\phi \in \mathbb{R}$ and the radial misalignment errors $\delta \in \mathbb{R}$ and $\epsilon \in \mathbb{R}$. The error ϕ appears when the double-prismatic joint is not perpendicularly connected. δ and ϵ represent the propagation of errors in the kinematic chain along the X_t- and Y_t-axis, respectively.

Considering the assembly errors, the homogeneous transformation matrix mapping the tool-tip frame (X_t, Y_t, Z_t) to the reference frame (X_o, Y_o, Z_o) is derived using the Denavit–Hartenberg method:

$$\boldsymbol{T}_t^o = \begin{bmatrix} -c_2c_4 & c_2s_4 & -s_2 & p_x \\ c_1s_4 - c_4s_1s_2 & c_1c_4 + s_2s_4s_1 & c_2s_1 & p_y \\ s_1s_4 + s_2c_4c_1 & c_4s_1 - s_2s_4c_1 & -c_1c_2 & p_z \\ 0 & 0 & 0 & 1 \end{bmatrix}, \tag{1}$$

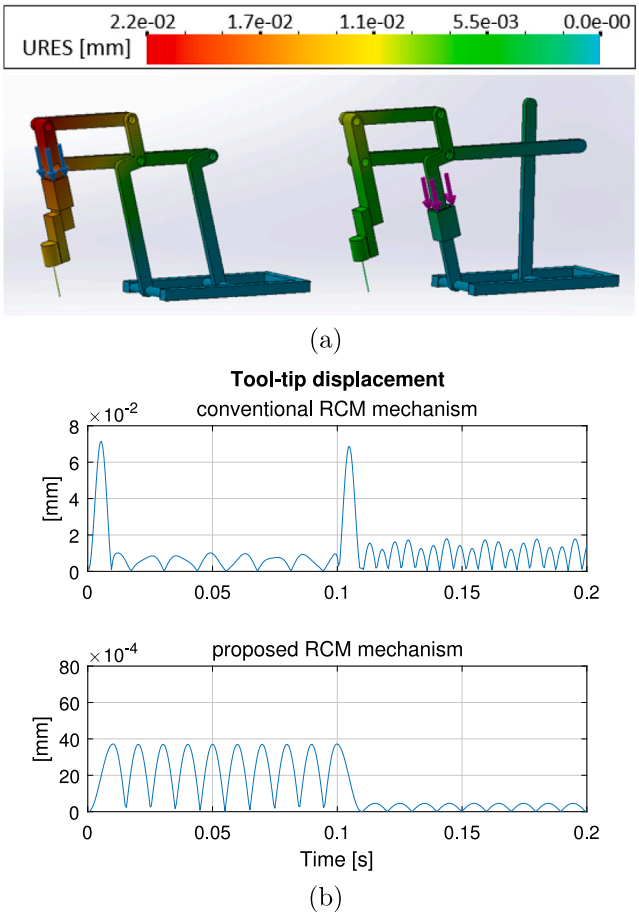

Fig. 2. Comparison of tool-tip displacements caused by tool acceleration in the conventional and the proposed double-parallelogram RCM mechanisms. (a) The mechanisms and their maximal deformations in the finite element simulation. Left: the conventional mechanism. Right: the proposed mechanism. (b) The tool-tip displacements of each mechanism.

where

$$p_x = s_2(d_3 - l_p) + c_2\delta + l_x(c_\phi - 1), \tag{2}$$

$$p_y = -s_1c_2(d_3 - l_p) + s_1s_2\delta + l_xs_1s_\phi - c_1\epsilon, \tag{3}$$

$$p_z = c_1c_2(d_3 - l_p) - c_1s_2\delta - l_xc_1s_\phi - s_1\epsilon. \tag{4}$$

Note that $s_\phi := sin(\phi)$ and $c_\phi := cos(\phi)$. Similarly, $s_i := sin(\theta_i)$ and $c_i := cos(\theta_i)$ for $i = \{1, 2, 3\}$. $\boldsymbol{p}_{tip} := (p_x, p_y, p_z)$, $\boldsymbol{p}_{tip} \in \mathbb{R}^3$, represents the tool-tip position in the reference frame.

When assembly errors are not considered, Eq. (1) can be reduced, and the result is identical to that of the conventional double-parallelogram RCM mechanism. In this case, the inverse kinematics is derived as

$$\theta_1 = -sgn(p_z)sin^{-1}\left(\frac{p_y}{\sqrt{p_y^2 + p_z^2}}\right), \tag{5}$$

$$\theta_2 = sgn(p_z)tan^{-1}\left(\frac{p_x}{\sqrt{p_y^2 + p_z^2}}\right), \tag{6}$$

$$d_3 = sgn(p_z)\sqrt{p_x^2 + p_y^2 + p_z^2} + l_p. \tag{7}$$

According to Eqs. (2)–(4), the RCM is voided as non-zero assembly errors are introduced. The attitude of the instrument is not affected by the assembly errors. This statement obviously holds for the radial misalignment errors δ and ϵ. On the other hand, the attitude of the instrument is copying the angles θ_1 and θ_2, which are actively controlled by the actuators. The angular misalignment error ϕ only affects the shape of the parallelogram, but not the joints θ_1 and θ_2. Thus, the amount of ϕ does not affect the attitude of the instrument.

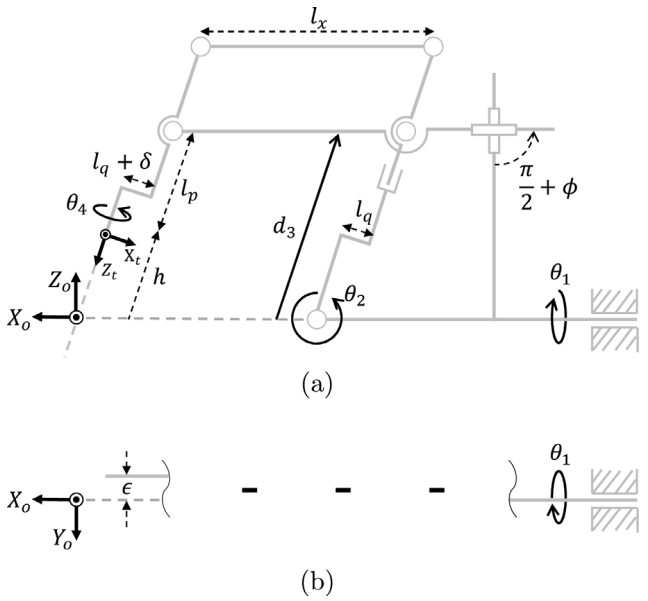

Fig. 3. Definition of the coordinate frames and kinematic parameters for the iORBIS robotic manipulator. (a) Side view. (b) Top view.

Table 1
Values of the kinematic parameters in the iORBIS manipulator.

Parameters	l_x	l_p	l_q
Values	200 mm	150 mm	37 mm

Using the forward kinematics (Eqs. (2)–(4)), the joint velocities in the actuator space is mapped to the tool-tip velocities:

$$\begin{bmatrix} \dot{p}_x \\ \dot{p}_y \\ \dot{p}_z \end{bmatrix} = \boldsymbol{J} \begin{bmatrix} \dot{\theta}_1 \\ \dot{\theta}_2 \\ \dot{d}_3 \end{bmatrix}, \tag{8}$$

where $\boldsymbol{J} \in \mathbb{R}^{3\times3}$ is the Jacobian matrix,

$$\boldsymbol{J} = \begin{bmatrix} 0 & c_2(d_3 - l_p) - s_2\delta & s_2 \\ -c_1c_2(d_3 - l_p) + c_1s_2\delta + l_xc_1s_\phi + s_1\epsilon & s_1s_2(d_3 - l_p) + s_1c_2\delta & -s_1c_2 \\ -s_1c_2(d_3 - l_p) + s_1s_2\delta + l_xs_1s_\phi - c_1\epsilon & -c_1s_2(d_3 - l_p) - c_1c_2\delta & c_1c_2 \end{bmatrix}. \tag{9}$$

By solving $det(\boldsymbol{J}) = 0$, three singularities are identified with the assumption of $\phi = 0$ and $\delta = \epsilon = 0$:

$$\begin{aligned} &\theta_2 = \{-\frac{\pi}{2}, \frac{\pi}{2}\} \\ &d_3 = l_p \end{aligned} \tag{10}$$

The singularities induced from θ_2 reflect the configurations where all four linkages of the parallelogram are colinear. The singularity at $d_3 = l_p$ indicates the case where the tool-tip is located at the RCM. This effect exists in all mechanically constrained RCM mechanisms.

2.3. RCM sensitivity analysis

A sensitivity analysis is performed to understand the effect of the assembly errors on the RCM precision and accuracy. For each type of misalignment, various amounts of error are applied, respectively. Utilizing the homogeneous transformation $\boldsymbol{T}_t^o$ (Eq. (1)), a set of instrument centerlines, obtained with a specific amount of error, is collected by uniformly commanding θ_1 and θ_2 in the range of ±45 degrees. We then determine the best location for the RCM based on these centerlines.

When n centerlines are collected, the best location for the RCM, $\boldsymbol{p}_{RCM} \in \mathbb{R}^3$, is defined as

$$\begin{aligned} \boldsymbol{p}_{RCM} &= \arg\min_{p} J(\boldsymbol{d}_1, \boldsymbol{d}_2, \dots, \boldsymbol{d}_n) \\ &= \arg\min_{p} \sqrt{\frac{\|\boldsymbol{d}_1\|_2^2 + \|\boldsymbol{d}_2\|_2^2 + \cdots + \|\boldsymbol{d}_n\|_2^2}{n}}, \end{aligned} \tag{11}$$

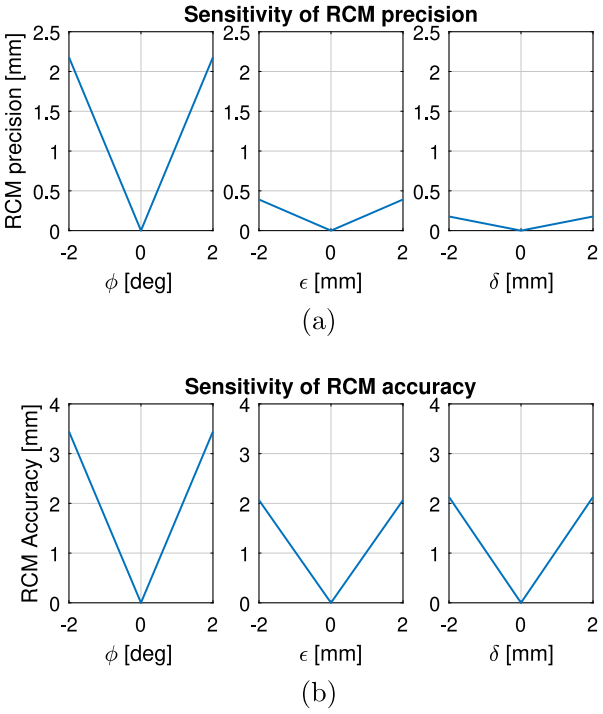

Fig. 4. Sensitivity of RCM performance to the assembly errors. (a) RCM precision. (b) RCM accuracy.

where $\left\|\boldsymbol{d}_j\right\|_2$ denotes the Euclidean distance from $\boldsymbol{p} \in \mathbb{R}^3$ to the centerline j, $1 \le j \le n$. Once $\boldsymbol{p}_{RCM}$ is solved, the RCM accuracy and precision are defined as $\|\boldsymbol{p}_{RCM}\|_2$ and the corresponding minimal cost $J(\boldsymbol{d}_1, \boldsymbol{d}_2, \ldots, \boldsymbol{d}_n)$, respectively.

The results of the RCM sensitivity analysis are shown in Fig. 4. As expected, a perfect RCM is obtained when zero assembly errors are applied. Both the RCM precision and accuracy are getting worse as the assembly errors increase. For the angular misalignment ϕ, the RCM precision and accuracy decrease around 1 and 1.7 mm per degree increase of $|\phi|$, respectively. For the radial misalignment ϵ, the RCM precision and accuracy decrease around 0.2 and 1 mm, respectively, when $|\epsilon|$ increases 1 mm. The effect of the radial misalignment δ in RCM accuracy is similar to that of ϵ. The RCM precision is less sensitive to the radial misalignment δ than to ϵ.

The RCM accuracy can be improved after kinematic calibration. Hence, the RCM performance mainly depends on its precision. In this sense, Fig. 4 suggests the importance of accurate alignment of the double-prismatic joint. It is also suggested to reduce the assembly error ϵ as it affects the RCM precision heavier than δ.

2.4. Assembly error estimation

Estimating and then correcting the misalignment errors after fabrication and assembly are essential to improve the RCM performance. For estimating the assembly errors, conventional methods usually require measurements of tool-tip positions in the reference frame (X_o, Y_o, Z_o). In practice, this requirement is challenging to meet because the measuring system has its own coordinate system. It is not trivial to determine the transformation matrix from the sensor's coordinate to the robot's coordinate when the assembly errors have not been calibrated.

In this work, a novel method is proposed for assembly error estimation based on contour distortion. Specifically, the iORBIS manipulator is commanded to follow several circular trajectories. The output trajectories are captured by a motion capture system. We then analyze the shape of the contours and use it as the feature to estimate the misalignment errors.

To start with, a circular trajectory parallel to the X_oY_o plane, with the center at (0,0,15) and the radius of 5 mm, is assigned as the reference. The $s_2(d_3 - l_p)$ term in Eq. (2) and the $-s_1c_2(d_3 - l_p)$ term in Eq. (3) indicate the desired circular contour appearing in the tool-tip trajectory. The effect of the misalignment error δ imposing on p_x is described by the $c_2\delta$ term in Eq. (2). Since c_2 is close to 1 when the circular contour is sufficiently small (i.e, θ_2 moves around 0 degrees), the misalignment error δ uniformly shifts the circular contour along the X_o-axis, as illustrated in the right subfigure of Fig. 5. The $l_x(c_\phi - 1)$ term in Eq. (2) is also negligible as the misalignment error ϕ is sufficiently small.

On the other hand, the $l_x s_1 s_\phi$ term in Eq. (3) distorts the circular contour when a non-zero misalignment error ϕ is considered, as illustrated in the left subfigure of Fig. 5. In Eq. (3), the $s_1 s_2 \delta$ term is negligible and the $c_1\epsilon$ term uniformly shifts the circular contour along the Y_o-axis. Thus, the assembly errors ϵ and δ do not distort the circular contour. By using these characteristics, it is possible to estimate the misalignment error ϕ from the distorted contour projected on the X_oY_o plane as those illustrated in Fig. 5.

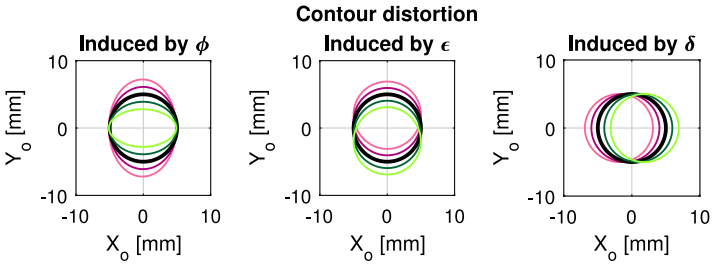

Fig. 5. Contour distortion, projected on the X_oY_o plane, induced by the assembly errors. Amount of error in degree or mm: 2( ), 1( ), 0( ), -1( ), and -2( ).

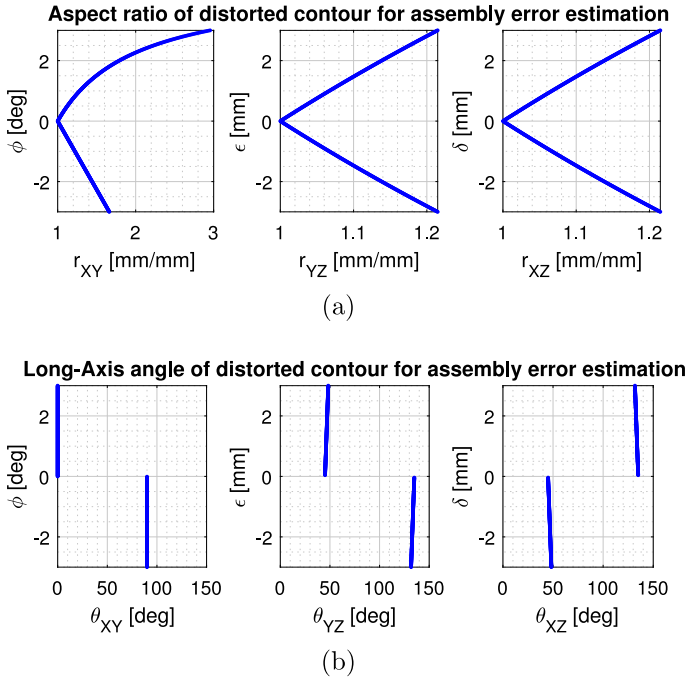

Fig. 6. Assembly error estimation using (a) aspect ratio and (b) long-axis angle of the distorted contour.

We propose using the aspect ratio of the distorted contour, r_{XY}, to estimate the amount of ϕ. The relationship between r_{XY} and ϕ is shown in Fig. 6. When ϕ equals zero, r_{XY} equals one, i.e., a perfect circular contour. r_{XY} grows up as $|\phi|$ increases. There is a nonlinear curve for positive ϕ and a linear curve for negative ϕ. This is because when $\phi > 0$, the length of the long-axis is approximately the same as the diameter of the desired circular contour. The length of the short-axis, otherwise, is decreased by $l_x s_1 s_\phi$. Thus, the aspect ratio of the distorted contour is a nonlinear function for positive ϕ. Oppositely, the length of the long-axis is increased by $l_x s_1 s_\phi$ and the length of the short-axis remains the same when $\phi < 0$. Therefore, the aspect ratio is linear for negative ϕ.

The misalignment ϕ has multiple solutions as given the aspect ratio of the distorted contour; one solution is positive, the other is negative. The long-axis angle θ_{XY} of the distorted contour is used to determine the sign of ϕ. θ_{XY} is 0 degrees for a positive ϕ and 90 degrees for a negative ϕ. Thus, we can check whether $\theta_{XY} > 45$ degrees to determine the sign of ϕ.

Similarly, the misalignment errors ϵ and δ can be estimated based on the distorted circular contour projected on the Y_oZ_o and X_oZ_o plane, respectively. Error estimating functions are established by fitting the data points in Fig. 6(a). Notably, the circular contour projected on the Y_oZ_o plane is affected by both misalignment errors ϵ and ϕ. Hence, $\hat{\phi}$ is set as an argument in the estimating function of ϵ. The fitting models and errors for each type of assembly errors are listed in Table 2.

The proposed method is evaluated by estimating $N = 20{,}000$ sets of assembly errors. In each set, the amount of assembly errors is randomly generated within the range designated in Table 2. The distorted contour is collected using the forward kinematics (Eq. (1)) and disturbed by measurement noises. The measurement noises, emulating the measuring error of the motion capture system, are uniformly distributed in the range of ±0.1 mm. The root-mean-square (RMS) errors of the estimates ϕ, ϵ, and δ are 1.8×10^{-2} degrees, 0.39 mm, and 0.15 mm, respectively. According to the sensitivity analysis presented in Section 2.3, the RCM precision and accuracy will be better than 0.5 mm after correcting the assembly errors based on the estimates.

Table 2
Fitting and testing results of assembly error estimation.

Estimating function	Range	Long-axis angle	Fitting model	Fitting error	Testing error
$\hat{\phi}(r_{XY})$ [deg]	$-3 \le \hat{\phi} < 0$	$\theta_{XY} > 45°$	poly3	2.4×10^{-7}	1.8×10^{-2}
	$0 < \hat{\phi} \le 3$	$\theta_{XY} < 45°$	poly3	1.8×10^{-2}	
$\hat{\epsilon}(\hat{\phi}, r_{YZ})$ [mm]	$-3 \le \hat{\epsilon} < 0$	$\theta_{YZ} > 90°$	poly55	1.2×10^{-1}	3.9×10^{-1}
	$0 < \hat{\epsilon} \le 3$	$\theta_{YZ} < 90°$	poly55	1.3×10^{-1}	
$\hat{\delta}(r_{XZ})$ [mm]	$-3 \le \hat{\delta} < 0$	$\theta_{XZ} < 90°$	poly3	2.0×10^{-5}	1.5×10^{-1}
	$0 < \hat{\delta} \le 3$	$\theta_{XZ} > 90°$	poly3	1.1×10^{-3}	

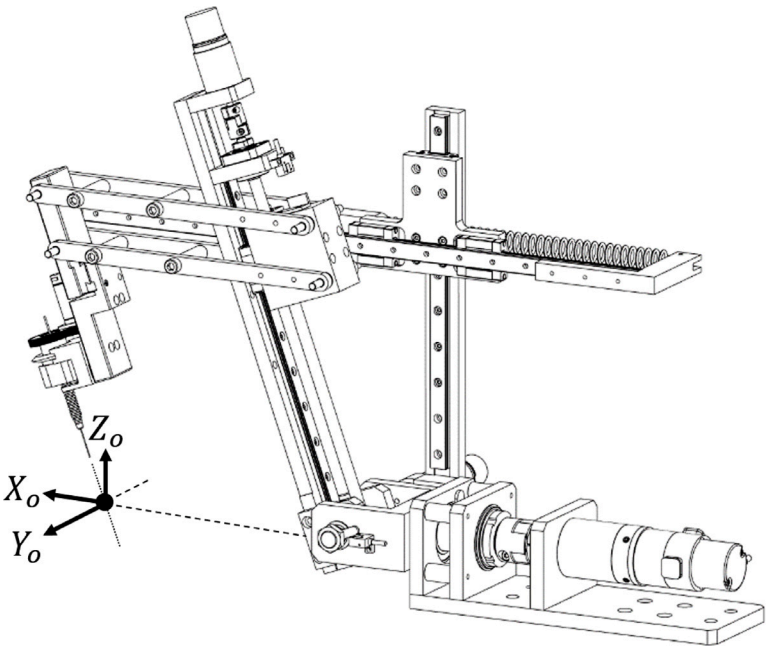

Fig. 7. Detailed design of the iORBIS robotic manipulator.

3. Mechanical design of the iORBIS

In this work, a novel intraocular robotic surgical system – the iORBIS – is developed. The mechanical design of the iORBIS, including the robotic manipulator and the automatic instrument changer, is described in this section.

3.1. Robotic manipulator

The detailed design of the robotic manipulator is shown in Fig. 7. The roll angle θ_1, which indicates the rotational motion about the X_o-axis, is actuated by a brush DC motor with harmonic gearing (Harmonic Drive RH-11D-3001-E100AL) to reduce the error caused by the mechanical backlash problem. A C-shape base is attached to the shaft of this motor. This base realizes the baseline EF as illustrated in Fig. 1(c). The pitch angle θ_2, which indicates the rotational motion about the Y_o-axis, is actuated by another brush DC motor (Faulhaber 2657W024CR, Planetary Gearhead 30/1 134:1, Encoder IE3-1024). This motor is fixed on the C-shape base and drives the deformation of the parallelogram. The tool translation, denoted as d_3, is actuated by a linear ball screw actuator with a 2 mm thread. The ball screw mechanism is driven by a brush DC motor (Faulhaber 2642W024CR, Encoder IE3-1024). The parallelogram structure is attached to the carriage of the linear actuator in order to actuate the translational motion of the instrument.

The double-prismatic joint is realized by two linear guides connected perpendicularly. The vertical rail is fixed on the C-shape base, representing the segment DF illustrated in Fig. 1(c). The horizontal rail is attached to the parallelogram structure, representing the segment CD. Besides, the right end of the horizontal rail is connected to the slider on the vertical rail using a spring. The spring force along the X_o-axis mitigates the mechanical backlash problem caused by the gearbox of θ_2 motor. The lengths of the horizontal and vertical rails are determined based on the desired moving ranges of the joints θ_2 and d_3. The vertical rail is longer than the maximum of d_3 to cover its range of motion fully. The length of the horizontal rail, on the other hand, is around twice the length of the vertical rail. This design allows the joint θ_2 moves to ± 45 degrees as the joint d_3 is moved to the highest position.

The effects of assembly errors are mitigated through our mechanical design. The horizontal linear guide uses two carriages to connect with the vertical linear guide. This design increases the structural rigidity against gravitational force and, thus, ensures the perpendicularity of the double-prismatic joint. In addition, a linear microstage (Misumi XFEES25), allowing fine adjustment within ±5 mm along the Y_t-axis, is installed at the end-effector such that the radial misalignment ϵ can be compensated for. This microstage, as not being actuated, is only with the weight of 30 g. As can be seen in Fig. 7, the design of the end effector still remains simple and lightweight. Finally, the radial misalignment δ is compensated for by including the estimated error in the design of the instrument holder, which is fabricated after the robotic manipulator. Specifically, the holder shifts the instrument centerline along the X_t-axis by $(l_q + \delta)$, as illustrated in Fig. 3.

3.2. Automatic instrument changer

With the simplified design near the end-effector after applying the proposed RCM mechanism, automatic instrument changing is made possible in the iORBIS. The specifications of the proposed instrument changing system are defined as being (1) able to automatically change instruments without the need for calibration during a surgical task; (2) able to accommodate the instruments of the diameter up to 10 mm; and (3) able to rotate the instrument about its centerline at the speed of 30 deg/s or faster.

Inspired by the work proposed in [37] and the automatic pen changing mechanism on a two-dimensional plotter (Roland DXY-1200), the developed automatic instrument changing system comprises two parts: instrument adapters and instrument holders. The instrument adapter creates a uniform interface between various surgical instruments and the instrument holder. The instrument holder clamps the surgical tool through the instrument adapter. Particularly, the instrument can be transferred from one holder to another empty holder once two holders are connected.

The detailed designs of the instrument adapter and instrument holder are shown in Fig. 8. Fig. 8(a) illustrates the components and assembly of the instrument adapter. The adapter consists of a pair of collet and nut, a coupler, and a gear. The ER-16 collet accepts instruments with a diameter ranging from 1 to 10 mm. A disk with V-shape edges forms the coupler. The coupler ensures that the instrument can be repeatedly held at the same height with regard to the holder. The distance between the tool-tip and the coupler is chosen as 100 mm. The gear is assembled with the coupler such that the joint θ_4 can be driven by a motor installed on the top of the instrument holder. The nut radially squeezes the collet and fixes it with the coupler. Once the adapter is assembled and locked with the instrument, all the components are coaxial with the centerline of the tool. The instrument holder (Fig. 8(b)) applies a spring force to clamp the surgical tool through the instrument adapter. When the holder carries the instrument, the clips are propped. The spring force induced by the displacements of the clips pushes the instrument inward. Hence, the instrument is self-aligning and self-centering via the V-groove method.

Automatic instrument changing is achieved by the clamping mechanism. The steps of picking an instrument from one holder to another are illustrated in Fig. 9. Note that the source and the target holders are identical. In Step 1, two holders are aligned face to face. In Step 2, the target holder is moved toward the source holder. Since the clips of the source holder are initially propped by the clamped surgical instrument, the clips of the target (empty) holder split the clips of the source holder as two holders are connecting. Once connected, the surgical instrument is clamped by the target holder (Step 3). After disconnecting two holders, the instrument is transferred and self-aligned (Steps 4 and 5). Similarly, the instrument will be picked up by the source holder if these two holders are connected again. This changing mechanism only requires a linear stage to align the holders. The linear stage is typically used to carry the robotic manipulator for aligning the RCM to the incision port. Hence, the proposed automatic instrument changer does not increase the complexity of the system.

A guideline to select the spring in the instrument holder is given as follows. The spring force must be sufficiently strong such that the instrument is stably clamped against gravitational and tool-tissue interaction forces. Specifically, the spring constant K_s is subject to the following constraint:

$$2 \cdot K_s \Delta l_s \cdot l_a sin(\theta_a) \geq \frac{(F_g + F_t)}{cos(\theta_i)} \cdot l_b sin(\theta_b), \tag{12}$$

where Δl_s is the compressed distance of the spring as the instrument is clamped; F_g and F_t are the gravitational and tool-tissue interaction forces applied to the instrument, respectively; l_a, l_b, θ_a, θ_b, and θ_i are the kinematic parameters as labeled in Fig. 10. The values of these parameters are listed in Table 3. Eq. (12) considers the worst case where the holder is facing the ground. We also assume that the tool-tissue interaction force along the same direction reaches its maximum, approximately 200 mN in eye surgery [45]. In this case, the gravitational and tool-tissue interaction forces are balanced by the spring force, and, thus, the spring constant K_s must be larger than 0.08 N/mm as the total weight of the instrument and instrument adapter is around 100 g. The value of K_s is selected as 0.27 N/mm to satisfy this constraint.

Once the spring is selected, the static force required to perform instrument changing is then analyzed. When two holders are connected as the steps shown in Fig. 9, the target (empty) holder splits the clips of the source holder until it clamps the instrument, and then pull the instrument out from the source holder. The instrument changing mechanism might fail if the linear stage cannot provide sufficiently large forces against the resisting forces produced by the springs.

The force required to clamp the instrument, F_{cn}, is a function of the distance between two holders:

$$F_{cn} = \begin{cases} F_{tgt} & \text{if } 45.0 > \Delta x > 43.7, \\ F_{tgt} + F_{src} & \text{if } 43.7 \geq \Delta x > 25.0, \end{cases} \tag{13}$$

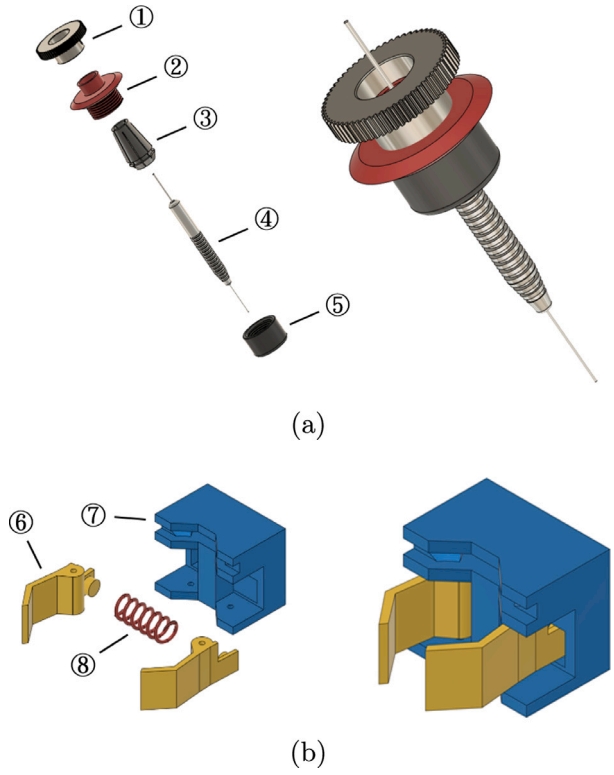

Fig. 8. Detailed design of the automatic instrument changer. (a) The instrument adapter: the ① gear, ② coupler, ③ collet, ④ instrument, and ⑤ nut. (b) The instrument holder: the ⑥ clips, ⑦ base, and ⑧ spring.

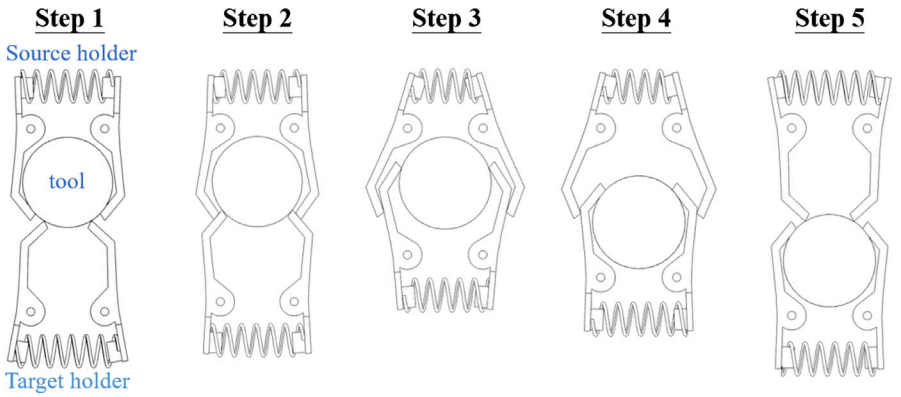

Fig. 9. Steps of picking up an instrument. Upper: source holder. Bottom: target holder.

where Δx in mm is defined as the distance between the pivots of two holders. F_{tgt} and F_{src} are the resisting forces produced by the spring on the target and the source holder, respectively:

$$F_{tgt} = -2\frac{K_s \Delta l_{s,tgt} \cdot l_a sin(\theta_{a,tgt})}{l_{b,tgt} sin(\theta_{b,tgt})} \cdot cos(\theta_{i,tgt}), \tag{14}$$

$$F_{src} = -2\frac{K_s \Delta l_{s,src} \cdot l_a sin(\theta_{a,src})}{l_{b,src} sin(\theta_{b,src})} \cdot [\frac{l_{inter} cos(\theta_{i,tgt})}{l_{b,tgt} sin(\theta_{b,tgt})} + cos(\theta_{i,src})]. \tag{15}$$

Note that $\Delta l_{s,tgt}$ and $\Delta l_{s,src}$ indicates Δl_s in the target and the source holder, respectively. The same nomenclature is applied to other kinematic parameters as well. l_{inter} represents the length of moment arm as the spring forces of the source holder apply to the clips of the target holder. All the kinematic parameters, except for l_a, are varying as Δx decreases.

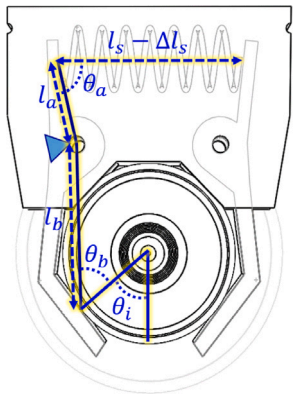

Fig. 10. Kinematic model of the instrument holder (top view).

Table 3
Values of the kinematic parameters in the automatic instrument changer.

Actions	l_s [mm]	l_a [mm]	l_b [mm]	Δl_s [mm]	θ_a [deg]	θ_b [deg]	θ_i [deg]
Holding	29.4	14.8	19.7	12.1	77	49	49

The variation of F_{cn} as Δx decreases from 45 to 25 mm is illustrated in Fig. 11(a). When $\Delta x > 43.7$ mm, the clips of the target holder are slightly propped by the instrument adapter, as Step 1 shown in Fig. 9. During this phase, only F_{tgt} is applied, and therefore the resisting forces are relatively small. F_{cn} is abruptly increased to 4.30 N at $\Delta x = 43.7$ mm. At this position (Step 2), the clips of the target holder start to split the clips of the source holder. The resisting forces are contributed by two springs. As Δx keeps decreasing, a discontinuous change of F_{cn} appears at $\Delta x = 37$ mm due to the switch of the contact points. Once $\Delta x = 33.7$ mm, however, the spring forces from the source holder start to assist the target holder to clamp the instrument. As a result, F_{cn} becomes negative (Step 3) until the instrument is completely clamped by the target holder at $\Delta x = 25$ mm.

The instrument changing process is halfway done. Next, the force required to pull out the instrument, after the instrument is clamped by the target holder, is solely contributed by the resisting force from the source holder:

$$F_{cn} = -2\frac{K_s \Delta l_{s,src} \cdot l_a sin(\theta_{a,src})}{l_{b,src} sin(\theta_{b,src})} \cdot cos(\theta_{i,src}). \tag{16}$$

In this case, Δx is increased from 25 to 45 mm. The corresponding F_{cn} is illustrated in Fig. 11(b). The resisting force remains around 0.32 N when $\Delta x < 36$ mm. When $\Delta x = 36$ mm, the clips of the source holder start to push the target holder outward (Step 4 in Fig. 9). Hence, F_{cn} becomes negative until the instrument is completely disconnected with the target holder at $\Delta x = 43$ mm (Step 5).

According to the above analysis, the maximum of F_{cn} is 4.30 N. This result is also roughly verified by an experiment performed on an electronic scale. In summary, the linear stage utilized for instrument changing must provide an axial static force large than 4.30 N.

3.3. System integration

The integration of the iORBIS system is as illustrated in Fig. 12. For automatic instrument changing, an empty instrument holder and the motor (Maxon 421721), which drives the rotational DoF about the instrument's centerline, are mounted on the robotic manipulator's end-effector. Each of the required surgical instruments is assembled with an instrument adapter and clamped by instrument holders on the tool shelf. The robotic manipulator is installed on an automated three-dimensional linear stage. Once a different instrument is requested, the robotic manipulator will first retract the instrument and move to the initial position ($\theta_1 = \theta_2$=0). Next, the automated linear stage shifts the robot to return the current instrument and then pick up the requested one. Upon completing the instrument changing process, the surgical task resumes. This process is typical in industrial applications. Therefore, we omit the details in this article.

In the iORBIS, a conventional three-dimensional linear stage is used for the convenience of prototypical experiments. The travel range of the linear stage should at least meet the specification of the automatic instrument changing system. The stage moving the robot along the X_o-axis is designed with an axial force up to 80 N. Thus, it provides a sufficiently large connecting force F_{cn} for instrument changing. Besides, we recommend using a lift stage for moving the robot along the Z_o-axis, as shown in Fig. 12, to avoid mechanical interference in the robot's workspace. The stage can be modified or augmented with more DoFs per the requirements in the operating room.

The brushed DC servo motors, which actuate the iORBIS system, are driven by H-bridge electronics. The angular position of each actuated joint is measured by optical encoders. Using a typical PID controller implemented on the National Instruments real-time

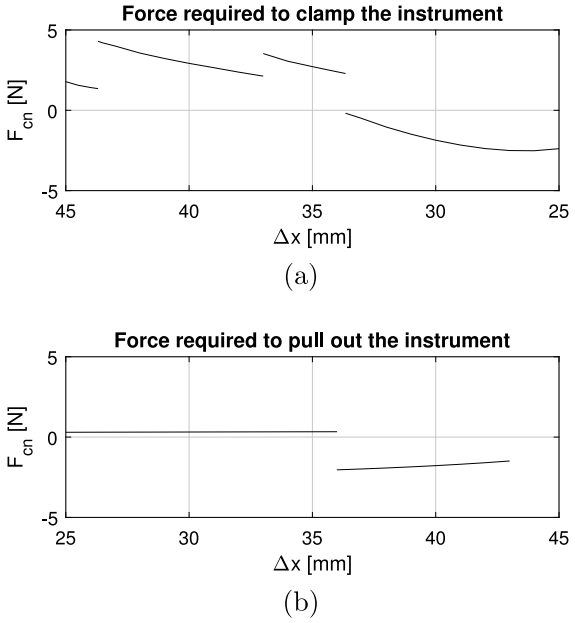

Fig. 11. Required forces to (a) clamp and (b) pull out the instrument from the source holder, respectively.

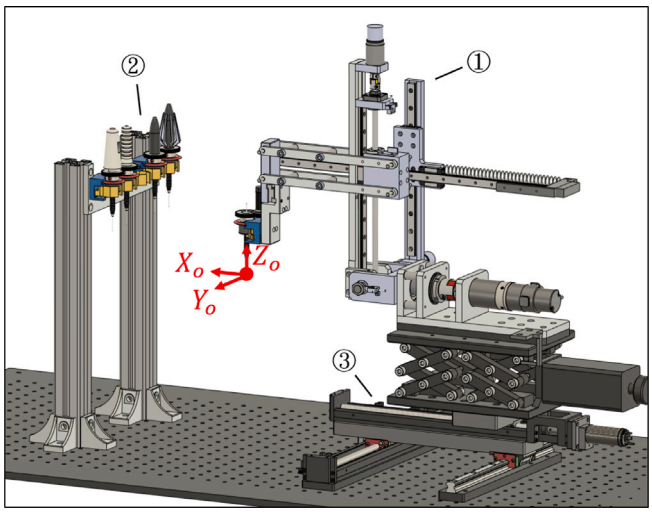

Fig. 12. Integration of ① the iORBIS robotic manipulator, ② the instrument shelf, and ③ the three-dimensional stage.

target with the sampling rate of 1 kHz, position control is achieved. The robot can be commanded to follow a predefined trajectory or controlled by a remote joystick under a master–slave configuration.

4. Prototype evaluation and discussion

In this section, a prototypical system is fabricated and assembled. We will evaluate the performance of the proposed RCM mechanism and the automatic instrument changer.

4.1. System prototype

The prototypical system is implemented as shown in Fig. 13 (Supplementary Video 1). For surgical automation, each motion axis is equipped with a photo-interrupter sensor to indicate the mechanical home position. The quantitative performance of each joint is measured, as listed in Table 4. The ranges of motion of the joints θ_1, θ_2, and d_3 are at least ±100 degrees, ±45 degrees, and 20 to

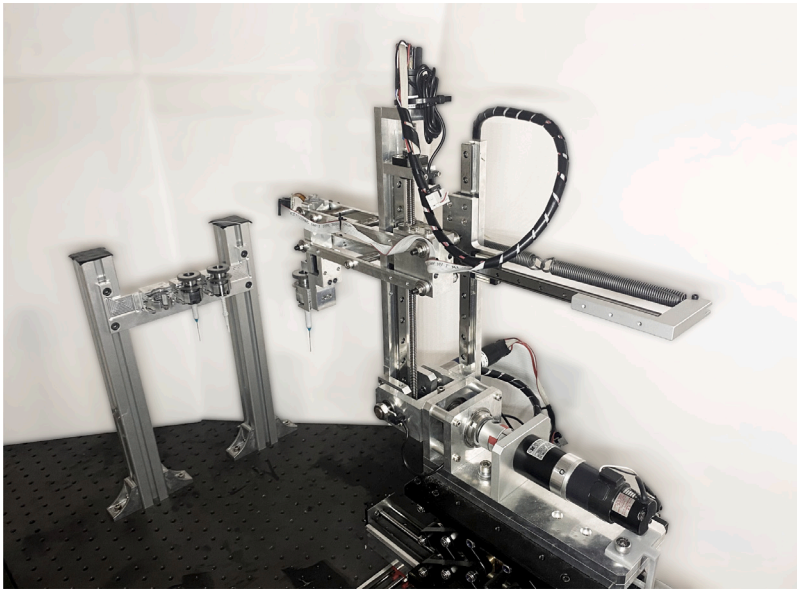

Fig. 13. Prototypical iORBIS system.

Table 4
Joint attributes of the iORBIS system.

Joint	Min limit	Max limit	Max velocity	Resolution
θ_1	−140 deg	132 deg	48.00 deg/s	0.90 mdeg
θ_2	−47 deg	47 deg	100.00 deg/s	0.66 mdeg
d_3	20 mm	170 mm	8.62 mm/s	0.49 μm
θ_4	−∞ deg	∞ deg	45.00 deg/s	0.85 mdeg
X_o	0 mm	200 mm	84.03 mm/s	0.49 μm
Y_o	0 mm	200 mm	84.03 mm/s	0.49 μm
Z_o	0 mm	75 mm	9.62 mm/s	25.52 μm

170 mm, respectively. In addition, the three-dimensional stage is able to translate the RCM in a 200 × 200 × 75 mm^3 workspace. Therefore, the iORBIS manipulator has a sufficiently large workspace for performing intraocular surgical procedures [13,27].

The joint accuracy and repeatability of the iORBIS manipulator are first evaluated. For each actuated joint, the manipulator is commanded to move forward and backward for $N = 10$ cycles. At every commanded position, the joint positioning errors are measured by the optical encoder. The average errors of each joint are shown in Fig. 14, in where the error bars represent the ranges of two standard deviations.

According to the ISO 230-2:2006 standard [46], the accuracy of the joints θ_1, θ_2, and d_3 is 0.19 degrees, 0.06 degrees, and 0.33 mm; and the repeatability is 0.02 degrees, 0.04 degrees, and 0.32 mm, respectively. The excellent repeatability of θ_1 and θ_2 is contributed by the anti-backlash mechanism using the harmonic gearing and preloaded spring, respectively. The accuracy of both joints can be improved further after a delicate calibration. A relatively large backlash is measured on the joint d_3 due to the ball screw mechanism. We recommend replacing the ball screw mechanism with a permanent magnet linear motor in future versions to solve this problem.

4.2. RCM performance

Applying the method presented in Section 2.4, the assembly errors are estimated and corrected. The resulted RCM performance is evaluated in this subsection. Conventional approaches for RCM evaluation involve using a third-party sensor like a stereo camera system to measure the pose of the end-effector [47]. However, these approaches require a complicated setup. The accuracy of the evaluation results is also subject to the measuring error of the sensory system. In this work, instead, we apply a mechanical approach to evaluate the RCM performance.

The experimental setup for evaluating the RCM performance is shown in Fig. 15. The iORBIS manipulator holds a needle made of aluminum with a diameter of 1 mm. The RCM of the robot is aligned to a circular hole in a thin aluminum plate. The needle penetrates the hole when the iORBIS manipulator moves around. A multimeter is used to detect whether the needle touches the edge of the hole during the motion. One probe of the multimeter is connected with the needle, and the other probe is connected with the plate. When the needle contacts with the edge of the hole, a conductive path is formed, and the multimeter will beep.

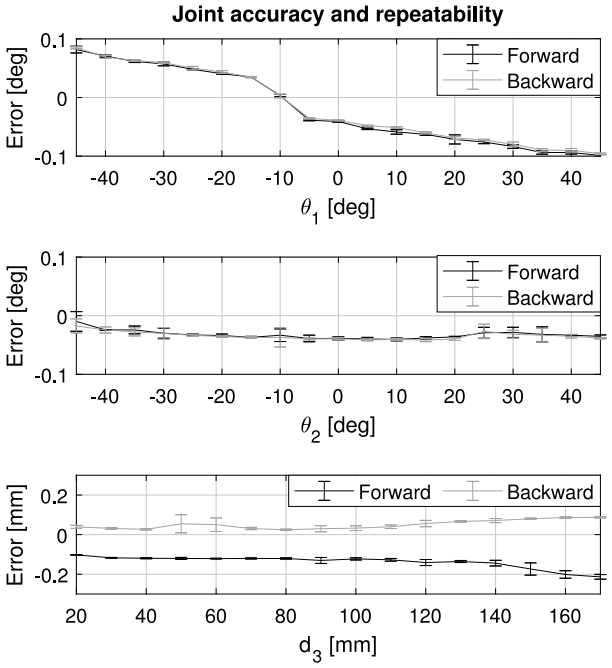

Fig. 14. Joint accuracy and repeatability of the iORBIS manipulator. The error bars represent the ranges of two standard deviations over $N = 10$ samples.

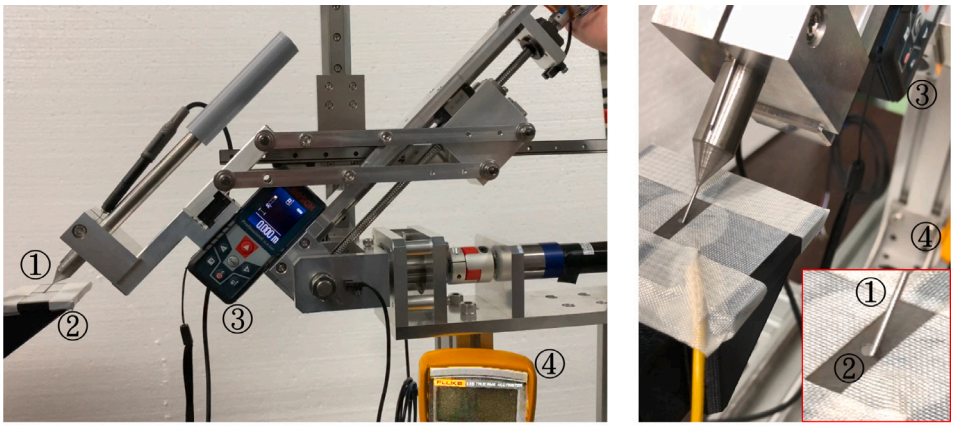

Fig. 15. Evaluation of the RCM: ① Needle held by the iORBIS with a diameter of 1 mm; ② A hole locating at the RCM with a diameter of 2 mm; ③ Inclinometer; ④ Multimeter detecting the contact between the needle and the edge of the hole.

In the experiment, the multimeter never beeps when the joints θ_1 and θ_2 move in the range of ±45 degrees (Supplementary Video 2). This result implies that the RCM precision is better than 0.5 mm since the hole in the aluminum plate is with a diameter of 2 mm.

4.3. Tool-tip positioning accuracy

Experiments are conducted to evaluate the tool-tip positioning accuracy in static pointing and dynamical trajectory tracking. In this experiment, the actual tool-tip positions are recorded using the PhaseSpace Motion Capture System [48] under the sampling rate of 26 Hz. The linear transformation between the sensor's coordinate and the robot's coordinate is established using Procrustes superimposition. Then, the l_2 error between the ideal and the measured position in the robot's frame is calculated to assess the tool-tip positioning accuracy.

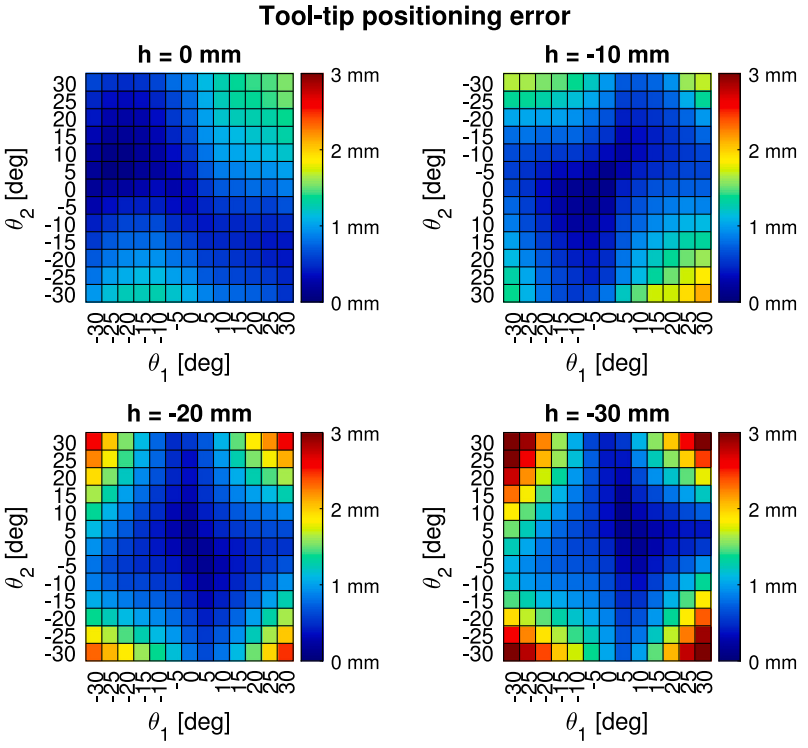

Fig. 16. Tool-tip positioning error of the iORBIS manipulator.

The robot is commanded to a set of points distributed in the robot's workspace to evaluate the static tool-tip positioning accuracy. Specifically, d_3 is commanded such that $h = d_3 - l_p = 0$ (the tool-tip is locating at the RCM), $h = -10$ (the tool-tip is 10 mm away from the RCM), $h = -20$, and $h = -30$ mm. For each set of h, the joints θ_1 and θ_2 move uniformly in the range of ± 30 degrees.

Fig. 16 shows the static tool-tip positioning accuracy. The errors are mostly less than 1.5 mm when the joints θ_1 and θ_2 move in the range of ± 20 degrees. When the tool-tip is locating at the RCM (h=0), the maximal error, 1.56 mm, occurs at $\theta_1 = \theta_2 = 30$ degrees. The worst-case happens when $h = -30$ mm, where the maximal error is around 3 mm. Note that the amount of the measured errors contains the sensory inaccuracy, especially when the marker is almost occluded as the joints θ_1 and θ_2 move to a large angle. Since the joint repeatability of the iORBIS manipulator has been shown excellent, the tool-tip accuracy can be improved further after a delicate calibration of kinematic parameters.

To assess the dynamical tool-tip positioning accuracy of the iORBIS manipulator, the robot is commanded such that the tool-tip is tracking a circular trajectory as illustrated in Fig. 17(a). The tracking error is shown in Fig. 17(b). The l_2 error, $\|e\|_2$, and the errors along each axis, e_x, e_y, e_z, are all less than 1 mm.

4.4. Performance of automatic instrument changer

The performance of the automatic instrument changer is evaluated in this subsection. An example of returning and picking up an instrument is shown in Fig. 18 (Supplementary Video 3). At $t = 0.00$ s, a tool adapter attached with a red marker is held by the iORBIS manipulator. By moving the iORBIS manipulator toward the instrument shelf using the three-dimensional actuated stage, this adapter is returned at $t = 1.92$ s. The returning process is completed, at $t = 3.90$ s, after moving the iORBIS manipulator back to the initial position. By repeating the same motion, the adapter is picked up again at $t = 7.80$ s. Although the automatic instrument changer is possible to work with a faster changing-speed, unnecessary vibrations would be induced when rapidly moving the iORBIS manipulator. Hence, we did not test the system with a faster motion. The experimental result has already confirmed that the time required for switching an instrument is less than ten seconds, which is fast enough for performing intraocular surgical tasks.

The repeatability of the automatic instrument changer is then assessed. The instrument adapter is returned and picked up from the three holders installed on the instrument shelf as the setup shown in Fig. 18. Each holder is tested for ten cycles. In this experiment, $\boldsymbol{p}_{tip} = (p_x, p_y, p_z)$, the position of the red marker representing the tool-tip, is recorded using the motion capture system. The standard deviations of p_x, p_y, p_z, and $\left\|\boldsymbol{p}_{tip}\right\|_2$ are listed in Table 5. The amounts of the standard deviations are all less than 0.1 mm, which is close to the resolution of the motion capture system. This result demonstrates the excellent repeatability of the proposed design.

The sensitivity of the automatic instrument changer is tested in this study. An offset is added to the three-dimensional actuated stage as the alignment error. The tool-tip position after changing with the specific stage alignment error is compared to the ideal

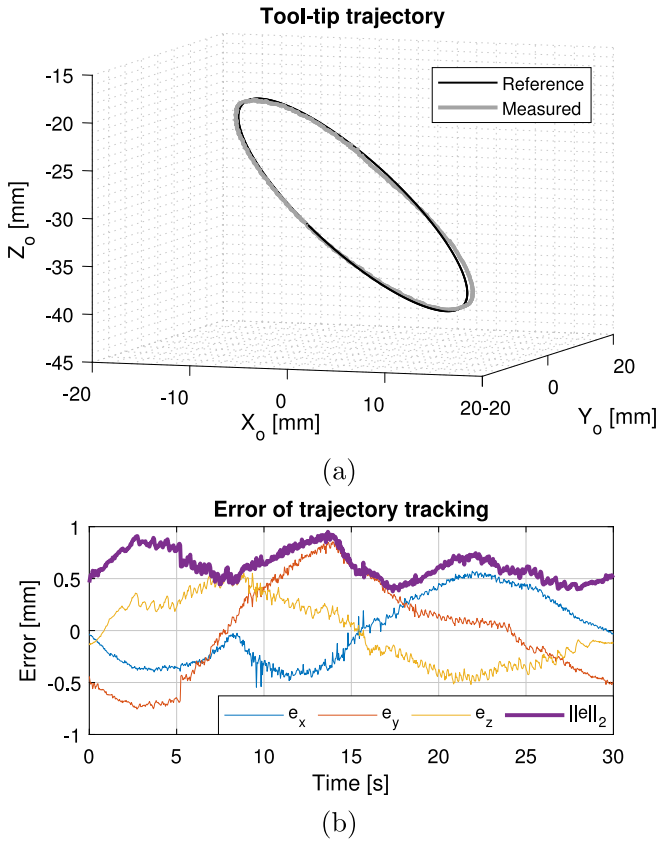

Fig. 17. Circular trajectory tracking. (a) Reference trajectory and measured tool-tip positions. (b) Tracking error.

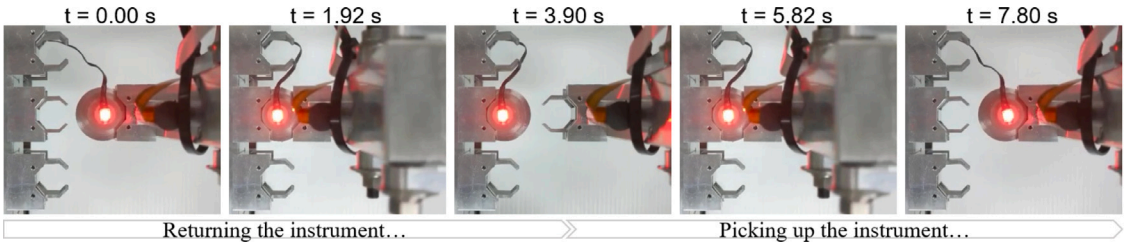

Fig. 18. Temporal screen shots of returning and picking up an instrument.

Table 5
Repeatability of automatic instrument changer.

Holder	$\sigma(p_x)$ [mm]	$\sigma(p_y)$ [mm]	$\sigma(p_z)$ [mm]	$\sigma(\|\mathbf{p}_{tip}\|_2)$ [mm]
#1	0.037	0.004	0.025	0.041
#2	0.011	0.010	0.036	0.015
#3	0.057	0.024	0.017	0.054

position. The alignment error is ranging from −1.5 to 1.5 mm and sampled every 0.25 mm. For each sampled point, the experiment is repeated for five times. The repeatability and accuracy of the linear stage are shown better than 20 and 50 μm, respectively (see Fig. 19). Compared to the amount of alignment errors, the positioning inaccuracies of the linear stage are negligible.

The results of the sensitivity study are presented in Fig. 19. When the stage alignment error is set as zero, the repeatability of the instrument changer is demonstrated. When the alignment error increases, the tool-tip positioning error slightly grows up. Particularly, the sensitivity along the X_o-axis is worse than the other two axes. The error variance along the X_o-axis is also larger than the others. These effects suggest that the holder might not stably clamp the instrument adapter if the distance between two

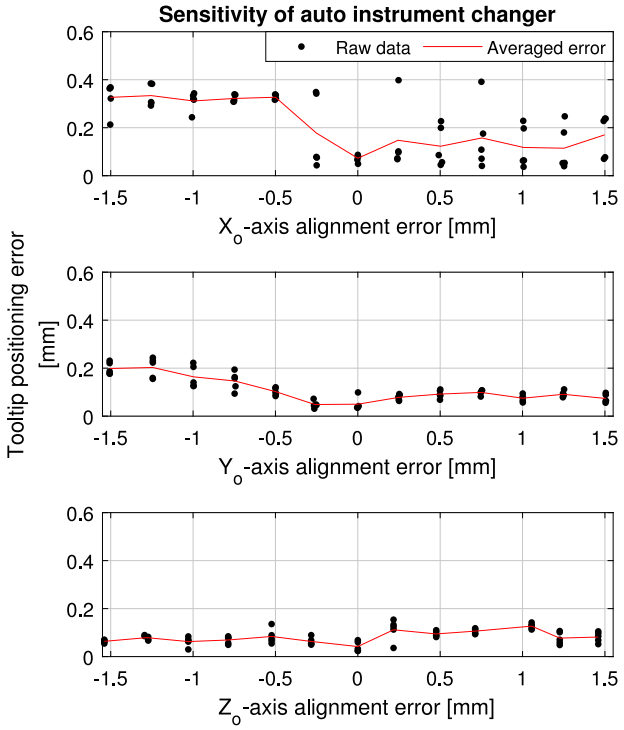

Fig. 19. Sensitivity of automatic instrument changer to the stage alignment errors.

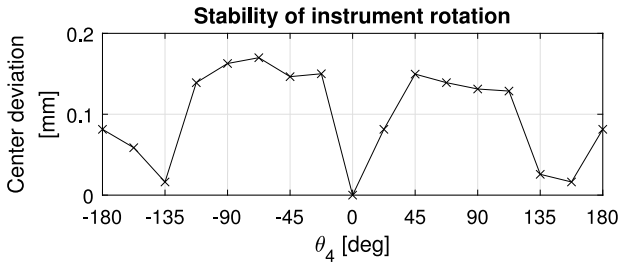

Fig. 20. Stability of instrument as the joint θ_4 rotates.

holders is not properly assigned. Generally speaking, the tool-tip positioning error is always less than 0.4 mm with the self-alignment design, even as the stage alignment error is up to 1.5 mm.

Last but not least, we evaluate the stability of the instrument when the joint θ_4 is rotating. Since it is not trivial to accurately attach a marker on the centerline of the instrument adapter, we install a micro camera in the adapter. An image-based method is used for the evaluation. In the experiment, a sheet printed with concentric circles is placed in front of the camera. The center of the concentric circles is aligned to the optical axis of the camera. The distance between the camera and the target is around 80 mm. We then rotate the joint θ_4 and record the deviations of the concentric circles. Ideally, the center of the concentric circles will show exactly at the center of the captured images no matter how the joint θ_4 rotates. The experimental result is shown in Fig. 20, in where the maximal deviation is measured around 0.17 mm. This result confirms that the instrument is stably held by the robot when the joint θ_4 is rotating.

5. Conclusion

The mechanical design of the intraOcular RoBotic Interventional System (iORBIS) is analyzed and evaluated in this work. With the novel parallelogram-based RCM mechanism, our system features distally-actuated instrument insertion and retraction. The simplified and compact design near the end-effector further enables the integration of an automatic instrument changing subsystem. The time required for returning an instrument and picking up another one is shown to be less than ten seconds.

The kinematic analysis regarding the proposed RCM mechanism is performed. In order to improve the RCM performance, a method is proposed to use the shape of distorted tool-tip trajectories for assembly error estimation. After correcting the misalignment

errors based on the estimated values, the RCM precision of the prototypical system is demonstrated as better than 0.5 mm. A series of experiments has verified the properties of the iORBIS system. The dynamical tool-tip positioning accuracy is better than 1 mm, while the tool-tip positioning error may be up to 3 mm as the manipulator moves to a large angle.

We are currently improving the iORBIS to meet the clinical requirement of 10 μm positioning accuracy. The inaccuracies caused by manufacturing errors and mechanical backlash will be reduced by revising the detailed design and actuation methods. A delicate kinematic calibration will be conducted. In the future, we will integrate other medical imaging modalities with the iORBIS and test its feasibility in performing intraocular surgical tasks. We will also evaluate the potential of converting the prototype into a commercial product.

Declaration of competing interest

One or more of the authors of this paper have disclosed potential or pertinent conflicts of interest, which may include receipt of payment, either direct or indirect, institutional support, or association with an entity in the biomedical field which may be perceived to have potential conflict of interest with this work. For full disclosure statements refer to https://doi.org/10.1016/j.mechmachtheory.2021.104568. Cheng-Wei Chen reports financial support was provided by Ministry of Science and Technology in Taiwan.

Appendix A. Supplementary data

Supplementary material related to this article can be found online at https://doi.org/10.1016/j.mechmachtheory.2021.104568.

References

[1] C. Bergeles, G.-Z. Yang, From passive tool holders to microsurgeons: safer, smaller, smarter surgical robots, IEEE Trans. Biomed. Eng. 61 (5) (2013) 1565–1576.
[2] J.I. Willems, A.M. Shin, D.M. Shin, A.T. Bishop, A.Y. Shin, A comparison of robotically assisted microsurgery versus manual microsurgery in challenging situations, Plast. Reconstr. Surg. 137 (4) (2016) 1317–1324.
[3] D. Zhang, J. Chen, W. Li, D.B. Salinas, G.-Z. Yang, A microsurgical robot research platform for robot-assisted microsurgery research and training, Int. J. Comput. Assist. Radiol. Surg. 15 (1) (2020) 15–25.
[4] R. Taylor, P. Jensen, L. Whitcomb, A. Barnes, R. Kumar, D. Stoianovici, P. Gupta, Z. Wang, E. Dejuan, L. Kavoussi, A steady-hand robotic system for microsurgical augmentation, Int. J. Robot. Res. 18 (12) (1999) 1201–1210.
[5] A. Üneri, M.A. Balicki, J. Handa, P. Gehlbach, R.H. Taylor, I. Iordachita, New steady-hand eye robot with micro-force sensing for vitreoretinal surgery, in: 2010 3rd IEEE RAS/EMBS International Conference on Biomedical Robotics and Biomechatronics, Tokyo, Japan, 2010, pp. 814–819.
[6] J. Song, B. Gonenc, J. Guo, I. Iordachita, Intraocular snake integrated with the steady-hand eye robot for assisted retinal microsurgery, in: 2017 IEEE International Conference on Robotics and Automation (ICRA), Singapore, 2017, pp. 6724–6729.
[7] R.A. MacLachlan, B.C. Becker, J.C. Tabarés, G.W. Podnar, L.A. Lobes Jr., C.N. Riviere, Micron: An actively stabilized handheld tool for microsurgery, IEEE Trans. Robot. 28 (1) (2011) 195–212.
[8] S. Yang, R.A. MacLachlan, C.N. Riviere, Manipulator design and operation of a six-degree-of-freedom handheld tremor-canceling microsurgical instrument, IEEE/ASME Trans. Mechatronics 20 (2) (2014) 761–772.
[9] M.A. Nasseri, M. Eder, S. Nair, E. Dean, M. Maier, D. Zapp, C.P. Lohmann, A. Knoll, The introduction of a new robot for assistance in ophthalmic surgery, in: 2013 35th Annual International Conference of the IEEE Engineering in Medicine and Biology Society (EMBC), Osaka, Japan, 2013, pp. 5682–5685.
[10] M.A. Nasseri, M. Eder, D. Eberts, S. Nair, M. Maier, D. Zapp, C.P. Lohmann, A. Knoll, Kinematics and dynamics analysis of a hybrid parallel-serial micromanipulator designed for biomedical applications, in: 2013 IEEE/ASME International Conference on Advanced Intelligent Mechatronics, Wollongong, Australia, 2013, pp. 293–299.
[11] M. Zhou, Q. Yu, K. Huang, S. Mahov, A. Eslami, M. Maier, C.P. Lohmann, N. Navab, D. Zapp, A. Knoll, M.A. Nasseri, Towards robotic-assisted subretinal injection: A hybrid parallel–serial robot system design and preliminary evaluation, IEEE Trans. Ind. Electron. 67 (8) (2019) 6617–6628.
[12] E. Rahimy, J. Wilson, T.-C. Tsao, S. Schwartz, J.-P. Hubschman, Robot-assisted intraocular surgery: Development of the IRISS and feasibility studies in an animal model, Eye 27 (8) (2013) 972–978.
[13] J.T. Wilson, M.J. Gerber, S.W. Prince, C.-W. Chen, S.D. Schwartz, J.-P. Hubschman, T.-C. Tsao, Intraocular robotic interventional surgical system (IRISS): Mechanical design, evaluation, and master–slave manipulation, Int. J. Med. Robot. Comput. Assist. Surg. 14 (1) (2018) e1842.
[14] M.D. de Smet, J.M. Stassen, T.C. Meenink, T. Janssens, V. Vanheukelom, G.J. Naus, M.J. Beelen, B. Jonckx, Release of experimental retinal vein occlusions by direct intraluminal injection of ocriplasmin, British J. Ophthalmol. 100 (12) (2016) 1742–1746.
[15] T. Edwards, K. Xue, H. Meenink, M. Beelen, G. Naus, M. Simunovic, M. Latasiewicz, A. Farmery, M. de Smet, R. MacLaren, First-in-human study of the safety and viability of intraocular robotic surgery, Nat. Biomed. Eng. 2 (9) (2018) 649–656.
[16] S. Charles, H. Das, T. Ohm, C. Boswell, G. Rodriguez, R. Steele, D. Istrate, Dexterity-enhanced telerobotic microsurgery, in: 1997 8th International Conference on Advanced Robotics, Monterey, CA, USA, 1997, pp. 5–10.
[17] C.-W. Chen, Y.-H. Lee, M.J. Gerber, H. Cheng, Y.-C. Yang, A. Govetto, A.A. Francone, S. Soatto, W.S. Grundfest, J.-P. Hubschman, et al., Intraocular robotic interventional surgical system (IRISS): Semi-automated OCT-guided cataract removal, Int. J. Med. Robot. Comput. Assist. Surg. 14 (6) (2018) e1949.
[18] C.-W. Chen, A.A. Francone, M.J. Gerber, Y.-H. Lee, A. Govetto, T.-C. Tsao, J.-P. Hubschman, Semiautomated optical coherence tomography-guided robotic surgery for porcine lens removal, J. Cataract Refract. Surg. 45 (11) (2019) 1665–1669.
[19] R.H. Taylor, J. Funda, D.D. Grossman, J.P. Karidis, D.A. LaRose, Remote center-of-motion robot for surgery, 1995, Google Patents, US Patent 5, 397, 323.
[20] B. Eldridge, K. Gruben, D. LaRose, J. Funda, S. Gomory, J. Karidis, G. McVicker, R. Taylor, J. Anderson, A remote center of motion robotic arm for computer assisted surgery, Robotica 14 (1) (1996) 103–109.
[21] D. Stoianovici, L.L. Whitcomb, D. Mazilu, R.H. Taylor, L.R. Kavoussi, Remote center of motion robotic system and method, 2006, Google Patents, US Patent 7, 021, 173.
[22] S. Aksungur, Remote center of motion (RCM) mechanisms for surgical operations, Int. J. Appl. Math. Electron. Comput. 3 (2) (2015) 119–126.
[23] P. Berkelman, E. Boidard, P. Cinquin, J. Troccaz, LER: The light endoscope robot, in: 2003 IEEE/RSJ International Conference on Intelligent Robots and Systems (IROS), Las Vegas, NV, USA, Vol. 3, 2003, pp. 2835–2840.
[24] M.J. Lum, J. Rosen, M.N. Sinanan, B. Hannaford, Optimization of a spherical mechanism for a minimally invasive surgical robot: Theoretical and experimental approaches, IEEE Trans. Biomed. Eng. 53 (7) (2006) 1440–1445.

[25] X. Zhang, C.A. Nelson, Kinematic analysis and optimization of a novel robot for surgical tool manipulation, J. Med. Dev. 2 (2) (2008) 021003.
[26] G. Zong, X. Pei, J. Yu, S. Bi, Classification and type synthesis of 1-DOF remote center of motion mechanisms, Mech. Mach. Theory 43 (12) (2008) 1585–1595.
[27] A. Gijbels, N. Wouters, P. Stalmans, H. Van Brussel, D. Reynaerts, E. Vander Poorten, Design and realisation of a novel robotic manipulator for retinal surgery, in: 2013 IEEE/RSJ International Conference on Intelligent Robots and Systems, Tokyo, Japan, 2013, pp. 3598–3603.
[28] A. Gijbels, E. Vander Poorten, P. Stalmans, H. Van Brussel, D. Reynaerts, Design of a teleoperated robotic system for retinal surgery, in: 2014 IEEE International Conference on Robotics and Automation (ICRA), Hong Kong, China, 2014, pp. 2357–2363.
[29] J. Li, G. Zhang, Y. Xing, H. Liu, S. Wang, A class of 2-degree-of-freedom planar remote center-of-motion mechanisms based on virtual parallelograms, J. Mech. Robot. 6 (3) (2014) 031014.
[30] K. Kong, J. Li, H. Zhang, J. Li, S. Wang, Kinematic design of a generalized double parallelogram based remote center-of-motion mechanism for minimally invasive surgical robot, J. Med. Dev. 10 (4) (2016) 041006.
[31] S. Nisar, T. Endo, F. Matsuno, Design and kinematic optimization of a two degrees-of-freedom planar remote center of motion mechanism for minimally invasive surgery manipulators, J. Mech. Robot. 9 (3) (2017) 031013.
[32] S. Nisar, T. Endo, F. Matsuno, Design and optimization of a 2-degree-of-freedom planar remote center of motion mechanism for surgical manipulators with smaller footprint, Mech. Mach. Theory 129 (2018) 148–161.
[33] M. Hadavand, A. Mirbagheri, S. Behzadipour, F. Farahmand, A novel remote center of motion mechanism for the force-reflective master robot of haptic tele-surgery systems, Int. J. Med. Robot. Comput. Assist. Surg. 10 (2) (2014) 129–139.
[34] G. Chen, J. Wang, H. Wang, A new type of planar two degree-of-freedom remote center-of-motion mechanism inspired by the peaucellier–lipkin straight-line linkage, J. Mech. Des. 141 (1) (2019) 015001.
[35] R.U. Ayres, Complexity, reliability, and design: Manufacturing implications, Manufact. Rev. 1 (1) (1988) 26–35.
[36] Y. Torres, S. Nadeau, K. Landau, Classification and quantification of human error in manufacturing: A case study in complex manual assembly, Appl. Sci. 11 (2) (2021) 749.
[37] M. Nambi, P.S. Bernstein, J.J. Abbott, A compact telemanipulated retinal-surgery system that uses commercially available instruments with a quick-change adapter, J. Med. Robot. Res. 1 (2) (2016) 1630001.
[38] Y. Ida, N. Sugita, T. Ueta, Y. Tamaki, K. Tanimoto, M. Mitsuishi, Microsurgical robotic system for vitreoretinal surgery, Int. J. Comput. Assist. Radiol. Surg. 7 (1) (2012) 27–34.
[39] X. He, D. Roppenecker, D. Gierlach, M. Balicki, K. Olds, P. Gehlbach, J. Handa, R. Taylor, I. Iordachita, Toward clinically applicable steady-hand eye robot for vitreoretinal surgery, in: ASME International Mechanical Engineering Congress and Exposition, Houston, Texas, USA, 2012, pp. 145–153.
[40] H. Yu, J.-H. Shen, K.M. Joos, N. Simaan, Design, calibration and preliminary testing of a robotic telemanipulator for OCT guided retinal surgery, in: 2013 IEEE International Conference on Robotics and Automation, Karlsruhe, Germany, 2013, pp. 225–231.
[41] H. Meenink, Vitreo-retinal eye surgery robot: Sustainable precision, (Ph.D. thesis), Eindhoven University of Technology, 2011.
[42] B.-S. Ryuh, S.M. Park, G.R. Pennock, An automatic tool changer and integrated software for a robotic die polishing station, Mech. Mach. Theory 41 (4) (2006) 415–432.
[43] R. Berenstein, A. Wallach, P.E. Moudio, P. Cuellar, K. Goldberg, An open-access passive modular tool changing system for mobile manipulation robots, in: 2018 IEEE 14th International Conference on Automation Science and Engineering (CASE), Munich, Germany, 2018, pp. 592–598.
[44] P. Garcia, J. Rosen, C. Kapoor, M. Noakes, G. Elbert, M. Treat, T. Ganous, M. Hanson, J. Manak, C. Hasser, D. Rohler, R. Satava, Trauma pod: A semi-automated telerobotic surgical system, Int. J. Med. Robot. Comput. Assist. Surg. 5 (2) (2009) 136–146.
[45] M.G. Urias, N. Patel, A. Ebrahimi, I. Iordachita, P.L. Gehlbach, Robotic retinal surgery impacts on scleral forces: in vivo study, Transl. Vis. Sci. Technol. 9 (10) (2020) 2.
[46] ISO 230-2:2006 test code for machine tools—part 2: Determination of accuracy and repeatability of positioning of numerically controlled axes, International Organization for Standardization Geneva.
[47] B. Rosa, C. Gruijthuijsen, B. Van Cleynenbreugel, J. Vander Sloten, D. Reynaerts, E. Vander Poorten, Estimation of optimal pivot point for remote center of motion alignment in surgery, Int. J. Comput. Assist. Radiol. Surg. 10 (2) (2015) 205–215.
[48] A. Aristidou, J. Lasenby, Motion capture with constrained inverse kinematics for real-time hand tracking, in: 2010 4th International Symposium on Communications, Control and Signal Processing (ISCCSP), Limassol, Cyprus, 2010, pp. 1–5.